J. Fluid Mech. (2003), *vol.* 495, *pp.* 343–368.
DOI: 10.1017/S0022112003006244 Printed in the United Kingdom

Large-eddy simulations of the wind-induced turbulent Ekman layer

By OLEG ZIKANOV[1], DONALD N. SLINN[2] AND MANHAR R. DHANAK[3]

[1]Department of Mechanical Engineering, University of Michigan – Dearborn, Dearborn, MI 48128-1491, USA

[2]Department of Civil and Coastal Engineering, University of Florida, Gainesville, FL 32611-6590, USA

[3]Department of Ocean Engineering, Florida Atlantic University, Boca Raton, FL 33431-0991, USA

(Received 29 May 2002 and in revised form 1 July 2003)

A turbulent Ekman layer created by a steady wind near the water surface is investigated using the numerical method of large-eddy simulations. The classical case of a flow unaffected by density stratification and surface waves is revisited to understand the internal structure of the flow and implications of the traditional assumptions of constant effective viscosity and the 'f-plane' approximation. A series of numerical experiments reveals that the Ekman solution needs correcting even in this case. The examination of the effective viscosity hypothesis confirms its validity but shows that the viscosity varies strongly with depth. It increases in the subsurface layer of thickness about 1/4 the turbulent length scale and decreases below this level. A Bessel function solution is proposed that corresponds to the approximate effective viscosity profile and matches with the LES results. Strong flow dependence on the latitude and wind direction is detected and explained by the effects of redistribution of turbulent kinetic energy between the velocity components and modification of the vertical transfer of turbulent momentum.

1. Introduction

In this paper, we consider the classical problem of a turbulent flow generated near the ocean surface by a steady wind stress in the presence of Earth's rotation. Interest in this flow goes back to Ekman's landmark work published in 1905. (An interesting historical review of Fridtjof Nansen's polar expedition and other events preceding Ekman's paper is given by Walker (1991).) Ekman assumed a balance between the Coriolis force, viscous friction and the pressure gradient, adopted the approximation of constant vertical eddy viscosity A_z, and derived a solution now known as the 'Ekman spiral'. In the case of a steady wind in the x-direction, the steady-state Ekman velocity profile in the open ocean is (for the northern hemisphere)

$$u = V_0 \cos\left(\frac{\pi}{4} + \frac{\pi}{D}z^*\right) \exp\left(-\frac{\pi}{D}z^*\right), \quad v = -V_0 \sin\left(\frac{\pi}{4} + \frac{\pi}{D}z^*\right) \exp\left(-\frac{\pi}{D}z^*\right). \quad (1.1)$$

Here u and v are the components of the mean horizontal velocity, z^* is the vertical coordinate directed downward, $V_0 = \sqrt{2}\pi\tau_0/Df\rho$ is the amplitude of the surface velocity, $D = \pi(2A_z/f)^{1/2}$ is the Ekman depth of exponential decay, τ_0 is the surface shear stress, and $f = 2\Omega \sin\lambda$ is the Coriolis parameter, with Ω and λ being, correspondingly, the Earth's rotation rate and latitude. According to the solution (1.1), the

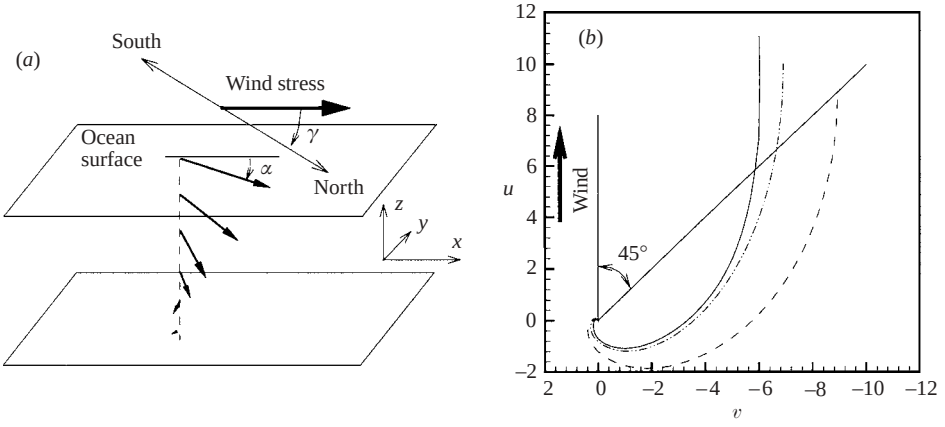

FIGURE 1. (*a*) Model geometry. (*b*) Time- and horizontally averaged hodographs of the horizontal current. ———, calculations at 90°-latitude; – – –, Ekman profile (1.1); – · · –, Bessel function solution (3.8) obtained with a piecewise-linear effective viscosity profile (see § 3.3 for details).

mean horizontal current spirals clockwise and decays exponentially with depth. At the surface, the velocity is directed at 45° to the right (northern hemisphere) or the left (southern hemisphere) of the wind direction. An illustration of the Ekman spiral is given in figure 1(*b*).

Simple, elegant, and clearly supported by laminar laboratory experiments, the Ekman model is, however, rather dissimilar to the actual turbulent flow near the ocean or lake surface. In fact, a persistent well-developed Ekman spiral has, probably, never been observed in field measurements (see Price & Sundermeyer 1999 for a review). The reason is, of course, that the over-simplified character of the model leads to significant inconsistencies between the predicted and actual flows. The most important ones are discussed below, and some of them are addressed in the later sections of this paper.

The basic assumptions of Ekman's model of a steady-state wind and absence of any geostrophic currents are never completely realized in the open ocean. Particularly important is the effect of transient winds. Attempts have been made to sort out the Ekman layer component of measured data (see, e.g., Price, Weller & Schudlich 1987; Chereskin & Roemmich 1991; Gnanadesikan & Weller 1995; Price & Sundermeyer 1999). Some important results have been found. In particular, the angle between the surface current and the wind was observed to be, typically, smaller than the 45° angle predicted by the Ekman model. A high degree of uncertainty, however, still remains associated with field observations of the phenomenon.

The assumption of a constant turbulent viscosity A_z is a crude approximation. In real flows, the intensity of turbulent momentum transport expressed by A_z is expected to vary with depth and time. This problem was recognized soon after Ekman's paper of 1905. Rossby & Montgomery (1935) tried to derive a realistic distribution $A_z(z^*)$ using the mixing-length theory. The mixing length ℓ was assumed to decrease with depth in the bulk flow but to increase linearly in a thin boundary layer near the surface. This adjustment resulted in a modification of the Ekman velocity profile. The angle between the wind and surface current was found to depend on the wind speed and latitude and, in most cases, to be slightly smaller than 45°.

Another attempt in this direction was made by Madsen (1977). His model, with the turbulent viscosity increasing linearly with depth, produced a rather unrealistic velocity profile with the surface velocity directed at an angle of about 10° to the wind direction.

Recent field measurements (see, e.g., Price *et al.* 1987; Schudlich & Price 1998; Price & Sundermeyer 1999) have revealed the importance of a serious limitation of the Ekman model, recognized by Ekman himself. The model ignores the profound effects of density stratification and buoyancy. Stable stratification can cause considerable (2 or 3 times) reduction of the depth of the Ekman layer. The wind-driven transport becomes trapped in a relatively shallow surface layer. On the other hand, evaporative cooling during the night time can initiate turbulent thermal convection that leads to the growth of the surface mixed layer and to release of the constraint imposed by stratification. A combination of the two effects is known to produce distinguishable diurnal oscillation of the flow (Price, Weller & Pinkel 1986). A turbulent convective layer under the surface can also be produced in shore regions during cold air outbreaks (Zikanov, Slinn & Dhanak 2002).

Another important flow mechanism is associated with surface gravity waves. The Lagrangian Stokes drift and associated Langmuir instability and turbulence generation have been a subject of field observations (see, e.g., Langmuir 1938; Thorpe 1984; Weller & Price 1988), theoretical modelling (Craik & Leibovich 1976), and numerical simulations (see McWilliams, Sullivan & Moeng 1997; Skyllingstad, Smith & Crawford 2000). It has been found that, under typical wave and wind conditions, increased turbulence intensity and coherent Langmuir circulation strongly affect the fundamental flow properties such as the mean velocity profiles and characteristics of turbulent momentum transport.

The classical Ekman model is based on the 'f-plane' approximation and, thus, neglects the possible influence of the horizontal (tangential to the Earth surface) component of the Earth's rotation vector and, thus, possible dependence of the flow on latitude and wind direction. Evidence that this simplification is not always justified was found in the systematic linear stability analysis of the Ekman profile by Leibovich & Lele (1985). Both for the atmospheric and for oceanic Ekman layer, the properties of unstable modes (growth rates and bands of unstable wavelengths) were found to be strongly affected by the horizontal component of the Earth's rotation vector. Further indications of the possible impact of the latitude and the wind direction on flow properties were obtained in a DNS study of the turbulent atmospheric Ekman layer by Coleman, Ferziger & Spalart (1990), where variations as large as 20% in the surface friction velocity and as large as 70% in the angle between the free-stream velocity and the wall shear stress were found.

There are other aspects of the flow behaviour that are disregarded by the classical Ekman model, such as bottom friction in flows in the shelf zone (see Pond & Pickard 1993, p. 117).

The purpose of this paper is to revisit the classical Ekman theory and investigate the consequences of two phenomena: variability of the turbulent viscosity coefficient and flow dependence on the latitude and wind direction. We separate these effects from the other complicating processes listed above. A turbulent shear flow generated by a constant surface wind stress is considered. Such an investigation is important for understanding the general properties of a variety of turbulent flows in the upper ocean. Furthermore, our formulation can be considered as a model of the offshore flows in fetch-limited wind conditions.

In § 2, we discuss the formulation of the problem, the large-eddy simulation (LES) approach, and the numerical method. The results of numerical experiments and an analytical solution are presented in § 3. Finally, concluding remarks are made in § 4.

2. Problem formulation

2.1. *Simplifying assumptions*

We simulate a turbulent flow in the upper (10 to 100 m deep) layer of the water column. The flow is generated by a steady and spatially homogeneous wind stress τ_0 applied at the water surface. We assume the following:

(i) The fluid is incompressible and neutrally stratified.

(ii) The flow is statistically homogeneous in the horizontal directions. This means that the effect of Ekman pumping is ignored.

(iii) The water surface is approximated by an impermeable flat lid. The Stokes drift and Langmuir turbulence due to the surface gravity waves are neglected.

(iv) Since the typical Reynolds number of the real ocean flow is very high (10^7 or higher based on the typical mean velocity and depth), we do not attempt to resolve the viscous boundary layer near the upper surface. Instead, the boundary condition is prescribed in the form of a constant shear stress. The molecular viscosity term is neglected in the equations. Only the momentum transfer produced by the turbulent stresses is taken into account. This corresponds to the assumption of infinite Reynolds number.

(v) The flow is assumed to be in the deep ocean, so no rigid bottom is included. The effect of the underlying water column is modelled by an idealized free-slip boundary condition discussed below.

A sketch of the model geometry is given in figure 1(*a*).

2.2. *Governing equations and boundary conditions*

The non-dimensional governing equations are

$$\frac{\partial u}{\partial t} + \boldsymbol{u}\cdot\nabla u = -\frac{\partial p}{\partial x} + \frac{\partial \tau_{1k}}{\partial x_k} + v - 2\Omega_{\tau y} w, \tag{2.1}$$

$$\frac{\partial v}{\partial t} + \boldsymbol{u}\cdot\nabla v = -\frac{\partial p}{\partial y} + \frac{\partial \tau_{2k}}{\partial x_k} - u + 2\Omega_{\tau x} w, \tag{2.2}$$

$$\frac{\partial w}{\partial t} + \boldsymbol{u}\cdot\nabla w = -\frac{\partial p}{\partial z} + \frac{\partial \tau_{3k}}{\partial x_k} - 2\Omega_{\tau x} v + 2\Omega_{\tau y} u, \tag{2.3}$$

$$\frac{\partial u}{\partial x} + \frac{\partial v}{\partial y} + \frac{\partial w}{\partial z} = 0, \tag{2.4}$$

where (u, v, w) are the velocity components, p is the pressure, and τ_{ik} is the subgrid-scale turbulent stress tensor. We use the Cartesian coordinate system with the origin at the base of the computational domain. The z-axis is pointed upward normal to the water surface and the x-axis is aligned with the direction of wind stress. The full Coriolis force is included so the f-plane approximation is not invoked. The Coriolis force associated with the tangential component $\boldsymbol{\Omega_\tau}$ of the Earth's rotation vector has the x- and y- (normal to the wind) non-dimensional components $\Omega_{\tau x} = (\frac{1}{2})\cot\lambda\cos\gamma$ and $\Omega_{\tau y} = (\frac{1}{2})\cot\lambda\sin\gamma$, where λ is the latitude, and γ is the angle between the wind direction (x-axis) and the direction of $\boldsymbol{\Omega_\tau}$ (south–north direction) (see figure 1*a*).

To non-dimensionalize the equations, we used the surface friction velocity $u_* = (\tau_0/\rho_0)^{1/2}$ as the typical velocity scale. Here, τ_0 is a constant wind stress applied

at the water surface and ρ_0 is the constant fluid density. For the time scale, we use the reciprocal Coriolis parameter $1/f = 1/2\Omega \sin\lambda$ (Ω is the angular velocity of the Earth's rotation). The turbulent length $L = u_*/f$ is used as the length scale, and the surface shear stress τ_0 serves as the scale for pressure p and the turbulent stresses τ_{ik}.

It can be noted that, under the assumptions made in our model, the non-dimensional solution at a given latitude and wind direction is representative of the solution with any value of the wind stress τ. Dimensional differences, of course, can be recovered by rescaling.

The equations (2.1)–(2.4) are solved numerically in a rectangular computational domain of dimensions $L_x \times L_y \times L_z$. Since the flow is assumed statistically homogeneous in the horizontal plane, periodic boundary conditions are applied in the x- and y-directions. At the bottom of the computational domain we impose the free-slip conditions

$$w = \tau_{13} = \tau_{23} = 0 \quad \text{at} \quad z = 0. \tag{2.5}$$

The upper surface is approximated by a flat impermeable lid, i.e. with a constant shear stress in the x-direction

$$w = 0, \quad \tau_{13} = \tau_0, \quad \tau_{23} = 0 \quad \text{at} \quad z = L_z. \tag{2.6}$$

Important for the subsequent discussion are the equations for horizontally averaged momentum. We use angle brackets $\langle \ldots \rangle$ to denote averaging over a horizontal plane, while $\langle \ldots \rangle_v$ and $\langle \ldots \rangle_t$ denote, respectively, volume averaging and a combination of horizontal and time averaging. The velocity field can be decomposed into the mean horizontal current

$$U(z,t) = \langle u \rangle, \quad V(z,t) = \langle v \rangle \tag{2.7}$$

and the perturbations

$$u' = u - U, \quad v' = v - V, \quad w' = w. \tag{2.8}$$

Taking the horizontal average of the momentum equations (2.1)–(2.3) we obtain

$$\frac{\partial U}{\partial t} = -\frac{\partial}{\partial z}[\langle u'w \rangle - \langle \tau_{13} \rangle] + V, \quad \frac{\partial V}{\partial t} = -\frac{\partial}{\partial z}[\langle v'w \rangle - \langle \tau_{23} \rangle] - U. \tag{2.9}$$

Assuming that the flow is steady in a statistical sense, time averaging leads to

$$\langle v \rangle_t = \frac{\partial}{\partial z}[\langle u'w \rangle_t - \langle \tau_{13} \rangle_t], \quad -\langle u \rangle_t = \frac{\partial}{\partial z}[\langle v'w \rangle_t - \langle \tau_{23} \rangle_t], \tag{2.10}$$

which expresses the balance between the Coriolis force and the vertical (resolved plus subgrid-scale) transfer of horizontal momentum. Allowing for the existence of a depth-dependent effective viscosity to parametrize the diffusive effects of the turbulent fluctuations we can express the total stresses as

$$\langle u'w \rangle_t - \langle \tau_{13} \rangle_t = -A_z(z)\frac{\mathrm{d}\langle u \rangle_t}{\mathrm{d}z}, \quad \langle v'w \rangle_t - \langle \tau_{23} \rangle_t = -A_z(z)\frac{\mathrm{d}\langle v \rangle_t}{\mathrm{d}z}, \tag{2.11}$$

so the momentum balance becomes

$$\frac{\mathrm{d}}{\mathrm{d}z}\left[A_z(z)\frac{\mathrm{d}\langle u \rangle_t}{\mathrm{d}z}\right] + \langle v \rangle_t = 0, \quad \frac{\mathrm{d}}{\mathrm{d}z}\left[A_z(z)\frac{\mathrm{d}\langle v \rangle_t}{\mathrm{d}z}\right] - \langle u \rangle_t = 0. \tag{2.12}$$

Below, we obtain $A_z(z)$ through averaging the calculated three-dimensional turbulent fields and use it to solve the model problem (2.12).

2.3. *Subgrid-scale closure*

In the large-eddy simulation, the turbulent stresses τ_{ij} are expressed in terms of the resolved velocity field. We use the dynamic subgrid-scale (SGS) closure (Germano *et al.* 1991 and Lilly 1992). At each time step, we calculate the resolved strain rate tensor

$$S_{ij} = \frac{1}{2}\left(\frac{\partial u_i}{\partial x_j} + \frac{\partial u_j}{\partial x_i}\right)$$

and approximate the deviatoric part of the turbulent stress tensor as

$$\tau_{ij} = 2\nu_t S_{ij}, \tag{2.13}$$

where $\nu_t(x, y, z, t)$ is the turbulent eddy viscosity.

The eddy viscosity is computed using the Smagorinski formula

$$\nu_t = C_s^2 \Delta^2 |S|, \tag{2.14}$$

where $\Delta = (\Delta_x \Delta_y \Delta_z)^{1/3}$ is the filter width based on the local grid spacing in each direction, and $|S| = (2S_{ij}S_{ij})^{1/2}$. The dynamically adjusted parameter $C_s(z, t)$ is calculated according to

$$C_s^2 = \frac{\langle L_{ij} M_{ij} \rangle}{\langle M_{ij} M_{ij} \rangle}. \tag{2.15}$$

The tensors L_{ij} and M_{ij} are determined after the application of the test filter with the width $\hat{\Delta} = (\hat{\Delta}_x \hat{\Delta}_y \Delta_z)^{1/3}$ with $\hat{\Delta}_x = 2\Delta_x$ and $\hat{\Delta}_y = 2\Delta_y$. The test filtering operation is performed in the horizontal plane using the spectral cut-off procedure. The formulae for L_{ij} and M_{ij} can be found, for example, in Lilly (1992).

2.4. *Numerical method*

A combination of pseudo-spectral and finite-difference numerical methods is applied for spatial discretization of the equations. In the two horizontal directions, the periodic boundary conditions allow use of the highly efficient Fourier pseudo-spectral technique based on the fast Fourier transform. Spatial derivatives are evaluated using the Fourier representation, while the multiplications required for nonlinear and SGS terms are performed in physical space. The aliasing errors generated in the transforms between the physical and spectral spaces are removed using the 2/3-rule technique.

In the vertical direction, the method of finite differences on a variable grid is used. The computational nodes are clustered near the upper surface. The z-coordinate is transformed according to

$$\zeta = \exp\left(\frac{z - L_z}{Z}\right), \tag{2.16}$$

where $Z \leqslant L_z$ is a constant stretching parameter. In the transformed coordinate, the equations are discretized using the second-order central differences on a staggered grid. Integer nodes $\zeta_i = i\Delta\zeta$, $i = 0, \ldots, N_z$ are used to calculate w, τ_{13}, and τ_{23} and to satisfy the vertical component of the momentum equation. The limits ζ_0 and ζ_{N_z} correspond to the lower and upper boundaries of the domain, respectively. All the other variables and equations are treated at the half-integer points $\zeta_{i+1/2} = (i + 1/2)\Delta\zeta$, $i = 0, \ldots, N_z - 1$. More details on the clustered grid technique used in this work can be found in Slinn & Riley (1998).

There is a certain controversy concerning LES simulations on anisotropic computational grids. For the dynamic Smagorinski model, the issue was addressed by Scotti, Meneveau & Fatica (1997). They found that the dynamic model automatically adjusts

to the grid anisotropy of the same kind as occurring in our case if the degree of anisotropy is not too high. In our calculations, $\Delta_x = \Delta_y$ and the ratio Δ_z/Δ_x varies between, approximately, 0.4 next to the surface and 1.9 at the bottom. Therefore, no anisotropy corrections were included in the dynamic procedure.

The time-marching scheme is the fully explicit time-splitting method based on the third-order Adams–Bashforth algorithm with variable time step. The size of the time increment is adjusted after each time step so that it tends to be the maximum increment allowed by the current stability conditions. Further details can be found in Slinn & Riley (1998). The only new feature added in the present work is that a single time step increase is restricted to 1% of the current time step.

To verify the numerical code we performed calculations of the laminar flow at low Reynolds number. The basic flow and its first instability were in agreement with the Ekman model and the linear stability analysis of Leibovich & Lele (1985).

3. Numerical experiments

3.1. *Procedure and parameters*

We performed a series of numerical experiments. Each experiment involved a simulation of the prolonged flow evolution for a particular set of physical and numerical parameters. The simulation started with a previously found turbulent flow field or with artificial initial conditions composed of the classical Ekman spiral and superimposed random weak velocity perturbations. Depending on the nature of the initial conditions, the initial flow adjustment occurred as a transformation of a turbulent flow or a rapid sequence of the laminar flow instability and transition to turbulence. In both cases, the adjustment was dominated by strong turbulent damping and typically required a time range shorter than 1/3 of the non-dimensional inertial time period $T_I = 2\pi$. The situation was clearly different from our test calculations of a laminar Ekman layer below the first stability limit, in which case very slowly decaying coherent inertial oscillations of the horizontal current were detected.

After completing the period of initial evolution, a developed turbulent flow was simulated and the turbulent flow statistics were collected for a time range of few T_I.

We carefully analysed the impact of the artificial boundary conditions at the lateral walls and at the bottom as well as the possible effects of the chosen numerical resolution. A detailed discussion is given in the Appendix. Here we mention that the domain dimensions $L_x \times L_y \times L_z = 1 \times 1 \times 1.5$ (measured in the turbulent length scale $L = u_*/f$) proved sufficient to minimize boundary effects. Computations with 64 collocation points in the horizontal directions and 120 vertical grid points provided results virtually indistinguishable from results obtained at higher resolution. Therefore, the above-mentioned parameters were adopted for the main body of the simulations. The grid stretching parameter was $Z = 1$.

The simulations were performed on a 600 MHz DEC ALPHA workstation and a CRAY T3E parallel computer equipped with 300 MHz SGI processors. For the latter, the numerical code was hand-parallelized. One time step required nearly 3 s and 0.7 s of CPU time of, respectively, the workstation and 24 parallel CRAY processors. Typical simulations were for 5×10^5 steps.

3.2. *Flow in the f-plane*

In this section, we give a detailed description of the results of the numerical experiment performed in the f-plane, i.e. at 90°-latitude. As a first illustration, figure 1(*b*) shows the hodograph of a time- and horizontally averaged horizontal current (the averaging

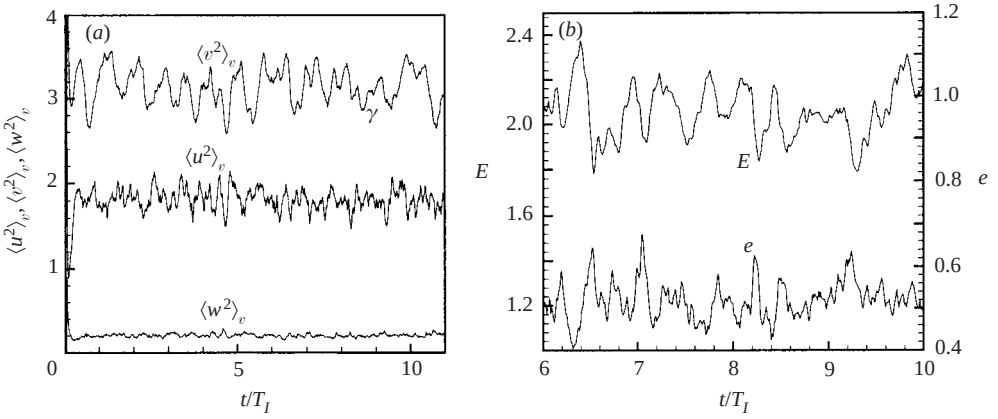

FIGURE 2. Volume-averaged kinetic energy as a function of time at the latitude 90°. (*a*) Total kinetic energy of each velocity component, $\langle u^2\rangle_v$, $\langle v^2\rangle_v$, and $\langle w^2\rangle_v$. (*b*) Kinetic energy of the mean horizontal current (E) and turbulent fluctuations (e).

procedure is discussed below) compared to the classical Ekman spiral (1.1). The surface velocity V_0 and the exponential decay depth D in (1.1) are chosen to match the surface velocity and the depth of exponential decay of the computed profile.

The current distribution differs significantly between the Ekman model and the computations. At the surface, the computed angle between the current and the wind stress is about 28.5°. We will see below that the angle changes with the latitude and wind direction. But, in agreement with the field observations, it remains smaller than the 45° predicted by the classical Ekman model.

3.2.1. *Flow evolution*

The evolution of global quantities of the developed turbulent flow is illustrated in figure 2. Figure 2(*a*) shows the volume-averaged kinetic energy of each velocity component $\langle u^2\rangle_v$, $\langle v^2\rangle_v$ and $\langle w^2\rangle_v$. The kinetic energy of the mean horizontal current $E = \langle U^2 + V^2\rangle_v/2$ and of the turbulent fluctuations $e = \langle u'^2 + v'^2 + w'^2\rangle_v/2$ are presented in figure 2(*b*). One can see that, during the entire experiment, the mean current contains about 80% of the flow kinetic energy.

The strong slow oscillations of volume-averaged quantities in figure 2 can be of purely stochastic nature, but, perhaps, can also include an inertial component correlating with the Earth's rotation. Even though inertial oscillations associated with the initial flow spin-up die off rather quickly (within $T_I/3$) due to strong turbulent damping, the possibility of an inertial component in the developed flow affected by the Coriolis force cannot be discarded outright. The issue has to be investigated carefully in a long run lasting, as in our experiment, many inertial time periods T_I. The question of inertial oscillations in a turbulent flow driven by steady forcing and influenced by the Earth's rotation has been raised a few times in the literature. For example, in DNS of the atmospheric Ekman layer, Coleman *et al.* (1990) did not find any predominance of the inertial frequency over other low frequencies. However, even in the presence of turbulent damping, we cannot exclude the possibility of such a predominance in the oceanic case, where there is no bottom friction.

To verify the possibility of predominantly inertial oscillations in our flow, the kinetic energy curves shown in figure 2(*a*, *b*) were interpolated into an equidistant grid and Fourier decomposed. The time interval $2T_I < t < 11T_I$ was investigated. No

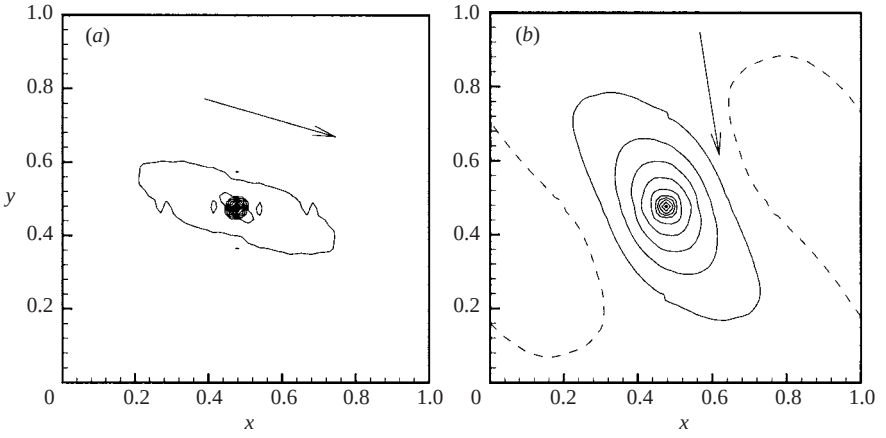

FIGURE 3. Two-point velocity correlations $(C_{11}+C_{22}+C_{33})/3$ (see (3.1)) in the developed turbulent flow at 90°-latitude. The correlations are calculated at (*a*) $z=L_z-0.04$ and (*b*) $z=L_z-0.22$ and averaged over the time period of $5T_I$. Contour step is 0.1. The contour levels range between 0.05 and 0.95 in (*a*) and between -0.05 (shown by dashed lines) and 0.95 in (*b*). Arrows show the direction of the time-averaged mean shear $\mathrm{d}(\langle u\rangle_t, \langle v\rangle_t)/\mathrm{d}z$.

dominance of the inertial frequency was detected. Therefore, we can conclude that the inertial oscillations, even if present, are absorbed by the stochastic background.

The precaution of time averaging over intervals consisting of an integer number of inertial periods thus becomes unnecessary. However, the averaging interval has to be taken large enough to eliminate the possible impact of the slow fluctuations shown in figure 2. In the Appendix, we show that averaging over $5T_I$ is accurate in presenting the first three statistical moments of the turbulent fluctuations. Intervals of this length were used in the bulk of the numerical experiments discussed in this paper.

3.2.2. *Velocity correlations*

The two-point velocity correlations

$$C_{ij}=\frac{\langle u_i'(\boldsymbol{x})u_j'(\boldsymbol{x}+\boldsymbol{r})\rangle_t}{\langle u_i'^2(\boldsymbol{x})\rangle_t^{1/2}\langle u_j'^2(\boldsymbol{x})\rangle_t^{1/2}} \tag{3.1}$$

were calculated on the horizontal planes at $z=L_z-0.04$ and $z=L_z-0.22$. In (3.1), $\boldsymbol{x}$ and $\boldsymbol{r}$ are two-dimensional horizontal vectors and u_i' are defined by (2.8). Figure 3 shows the summed correlation coefficients $(C_{11}+C_{22}+C_{33})/3$ calculated for the developed turbulent flow fields and time-averaged over $5T_I$. The point $\boldsymbol{r}=0$ is translated into the centre of the domain.

Visual investigation of snapshots of the velocity and vorticity fields and of instantaneous spatial correlations (not shown here) did not reveal any organized large-scale structures in the developed turbulent flow. The correlation contours in figure 3 support this observation. Both at $z=L_z-0.04$ and $z=L_z-0.22$, the direction of maximum coherence is very close to the direction of time-averaged vertical gradient of mean velocity $\mathrm{d}(\langle u\rangle_t, \langle v\rangle_t)/\mathrm{d}z$ (shown by the arrows). This indicates that vortex stretching by the mean shear is the reason for the elongation of the correlation contours.

Comparing the plots in figures 3(*a*) and 3(*b*) we find that, at larger depth, the flow becomes more isotropic and correlated over larger distances. This can be explained, respectively, by the decrease of the mean shear and the growth of the typical size of turbulent eddies with depth. Another important conclusion, which can be drawn

from the plots in figure 3, is that the horizontal dimensions of the computational domain are large enough to avoid any serious impact of the periodic boundaries on the turbulent fluctuations.

3.2.3. *Vertical profiles*

In this section we present the horizontally and time-averaged vertical profiles of the flow properties. The time-averaging is over $2T_I < t < 7T_I$ (cf. figure 2).

The mean horizontal velocity is shown in figure 4(a) in component form and in figure 1(b) as a hodograph. It must be stressed that, in our model, the shape of the mean current profile is dictated solely by the Ekman mechanism, i.e. by the balance between the vertical momentum transfer and the Coriolis force. We ignore potentially important factors such as density stratification, convection, and Langmuir turbulence. It has been shown (see, e.g., Price & Sundermeyer 1999) that stratification leads to the 'flattening' of the Ekman profile, while Langmuir turbulence (see McWilliams *et al.* 1997) and convection enhance the vertical mixing and, thus, lead to a more vertically uniform current.

To quantify the difference between the computed and theoretical profiles we calculated the depth distributions of the angle $\alpha(z)$ between the mean current $(\langle u\rangle_t, \langle v\rangle_t)$ and the wind direction (x-axis), and of the speed of the current $S = (\langle u\rangle_t^2 + \langle v\rangle_t^2)^{1/2}$ (see figure 1a). In figure 4(b), they are compared with the corresponding Ekman solutions $\alpha_E = \frac{1}{4}\pi + (\pi/D)(L_z - z)$ and $S_E(z) = V_0 \exp[-(\pi/D)(L_z - z)]$. Only the upper part $z > 0.5$ of the computational domain is shown since the weakness of the current at $z < 0.5$ renders the reliable evaluation of the characteristics of the computed current impossible. The surface velocity V_0 and the Ekman depth D used for the theoretical solution are chosen to match the surface velocity and the depth of exponential decay of the computed current (i.e. the depth where the current speed is equal to $V_{surface}\mathrm{e}^{-\pi}$).

One can see in figure 4(b) that, for the angle α, the computed and theoretical curves are fairly close. The current obtained in the simulations rotates in accordance with Ekman's predictions. The only really meaningful deviation is in the thin (about 0.05 turbulent lengths) surface layer. The difference in the current speed is more dramatic. For approximately $1.4 < z < 1.5$, the amplitude of the computed current decays much faster than the amplitude of the Ekman solution. As a result, the Ekman model over-estimates the current speed in the upper part of the flow.

Further comparison is made in figure 4(c). The coefficient (Price & Sundermeyer 1999)

$$F_l = \frac{\mathrm{d}S}{\mathrm{d}z}\left(S\frac{\mathrm{d}\alpha}{\mathrm{d}z}\right)^{-1} \tag{3.2}$$

is shown as a function of depth. For the Ekman spiral (1.1), the coefficient is $F_l \equiv 1$. Overall values between 2 and 3 were observed in oceanic flows with stable density stratification (Price & Sundermeyer 1999). One can see in figure 4(c) that the calculated F_l is close to the Ekman value. An exception is the thin subsurface layer, where markedly increased F_l can be attributed to the growth of $\mathrm{d}S/\mathrm{d}z$.

The profiles of root-mean-square turbulent velocity fluctuations are shown in figure 4(d). The larger part of the turbulent kinetic energy is contained in the area of strong shear in the upper third of the computational domain. The turbulent eddies, however, seem to penetrate deeper into the water column and, according to figures 4(d) and 4(a), have significant intensity in the region where the mean shear is small.

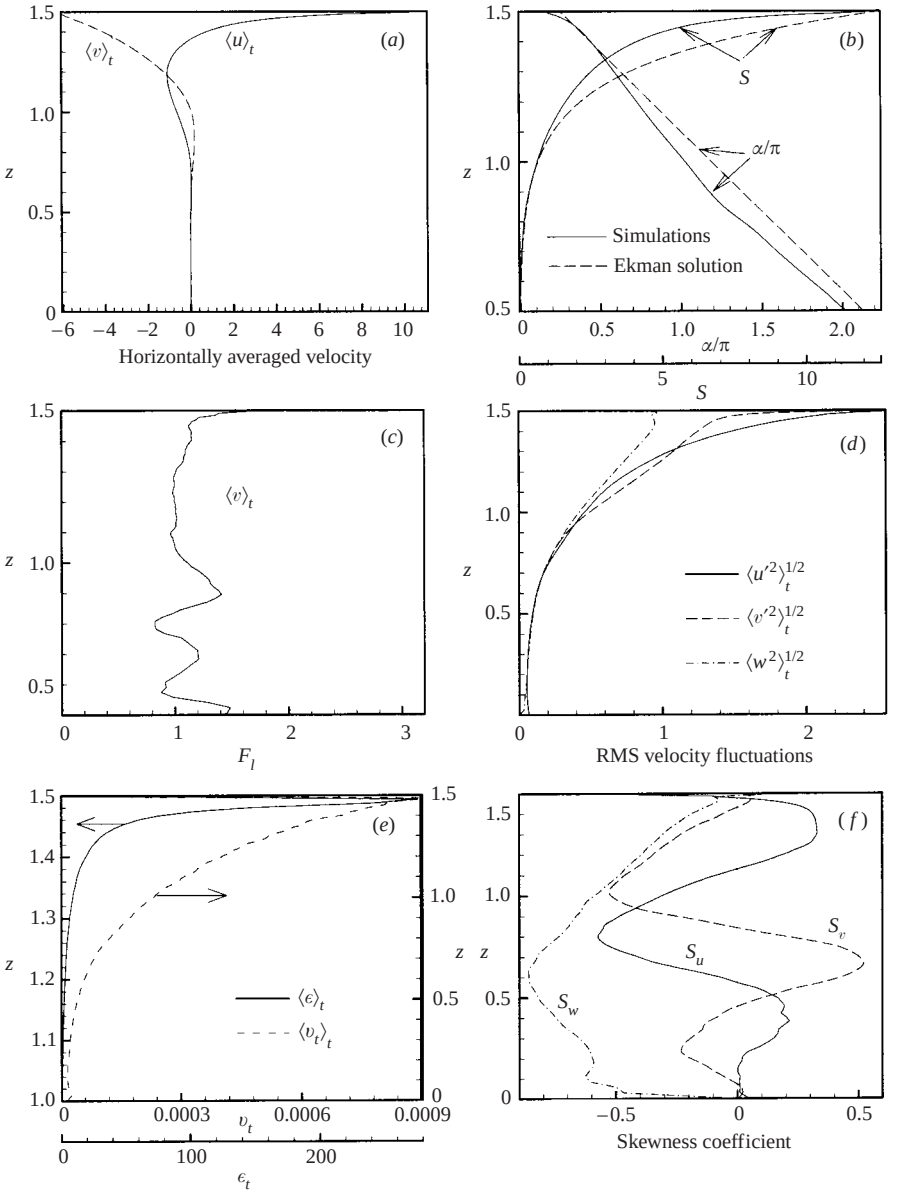

FIGURE 4. Horizontally and time-averaged profiles calculated in the developed turbulent flow at 90°-latitude. (*a*) Components of the mean horizontal current $\langle u\rangle_t$ and $\langle v\rangle_t$; (*b*) angle α between $(\langle u\rangle_t, \langle v\rangle_t)$ and the wind direction and the speed of current S; (*c*) coefficient F_l (3.2); (*d*) root-mean-square velocity fluctuations; (*e*) mean turbulent eddy viscosity ν_t (2.14) and the rate of subgrid-scale kinetic energy dissipation ϵ_t (3.3) (note different vertical and horizontal scales used to plot ν_t and ϵ_t); (*f*) skewness coefficients (3.4) of the velocity components.

Figure 4(*e*) shows the vertical profile of the rate of kinetic energy dissipation determined from

$$\langle \epsilon \rangle_t = -\langle \tau_{ij} S_{ij} \rangle_t. \tag{3.3}$$

The dissipation is concentrated near the surface, the degree of concentration being much higher than for the turbulent kinetic energy or the mean shear. This feature

can be explained in many different ways. In particular, we conclude that the typical size of turbulent eddies grows with depth (cf. velocity correlations on figure 3). This leads to the decrease of the amplitude of the strain rate components S_{ij} and to the decrease of the turbulent eddy viscosity coefficient ν_t. As an illustration, the time- and horizontally averaged profile of ν_t is presented in figure 4(*e*). Note that ν_t represents turbulent diffusivity at the subgrid scales and, thus, is completely different from the effective viscosity $A_z(z)$ discussed below that represents bulk diffusivity at both resolved and subgrid scales.

Further information about the resolved turbulent fluctuations is provided by the time- and horizontally averaged skewness coefficients

$$S_u = \frac{\langle (u')^3 \rangle_t}{\langle (u')^2 \rangle_t^{3/2}}, \quad S_v = \frac{\langle (v')^3 \rangle_t}{\langle (v')^2 \rangle_t^{3/2}}, \quad S_w = \frac{\langle (w)^3 \rangle_t}{\langle (w)^2 \rangle_t^{3/2}} \tag{3.4}$$

presented in figure 4(*f*). Positive or negative skewness means more frequent large excursions of the field variable in, respectively, positive or negative directions. One can see in figure 4(*f*) that the sign of S_u and S_v approximately follows the sign of, respectively, $\langle u \rangle_t$ and $\langle v \rangle_t$. This indicates that the strong turbulent bursts are more often in the direction of the mean flow than opposite to it. The negative sign of S_w shows that the localized descending motions are somewhat predominant over the ascending ones.

3.2.4. *Vertical stress and effective viscosity*

Figure 5(*a*, *b*) shows profiles of horizontally and time-averaged vertical stresses. One can see that the mean Reynolds stresses $\langle u'w \rangle_t$ and $\langle v'w \rangle_t$ are considerably stronger than the corresponding subgrid-scale stresses $\langle \tau_{13} \rangle_t$ and $\langle \tau_{23} \rangle_t$. Most of the vertical momentum transport in our model is carried by the turbulent motions at resolved length scales.

One of the principal goals of our simulations is to revisit the effective viscosity concept applied to the Ekman layer problem throughout its almost century-long history. In general, the existence of a single coefficient or even a single function of depth that systematically relates the mean total stress to the mean shear is questionable. The momentum transport is affected by the turbulent motions in the entire range of length and time scales of the flow. We can only hope that in a particular case, such as the Ekman flow, the mean flow profile can provide sufficient information for a meaningful effective viscosity model.

We start by verifying whether the mean total stress vector $(-\langle \tau_{13} + u'w \rangle_t, \langle -\tau_{23} + v'w \rangle_t)$ is aligned with the mean shear $(\mathrm{d}\langle u \rangle_t/\mathrm{d}z, \mathrm{d}\langle v \rangle_t/\mathrm{d}z)$. Figure 5(*c*) demonstrates the angles β_1 and β_2 between, respectively, each of these vectors and the wind direction. The alignment is nearly perfect. We can justifiably apply the effective viscosity model to describe the mean flow. For comparison, figure 5(*c*) includes the angle $\beta_E = (\pi/D)(L_z - z)$ that describes the rotation of the mean shear vector in the Ekman profile (1.1). There is a fairly good agreement between our computations and the Ekman model.

As a second step, we assume that the effective viscosity is a function of depth and evaluate it using the computed mean shear and total stress profiles as

$$A_z(z) = \frac{\left[\langle -\tau_{13} + u'w \rangle_t^2 + \langle -\tau_{23} + v'w \rangle_t^2\right]^{1/2}}{[(\mathrm{d}\langle u \rangle_t/\mathrm{d}z)^2 + (\mathrm{d}\langle v \rangle_t/\mathrm{d}z)^2]^{1/2}}. \tag{3.5}$$

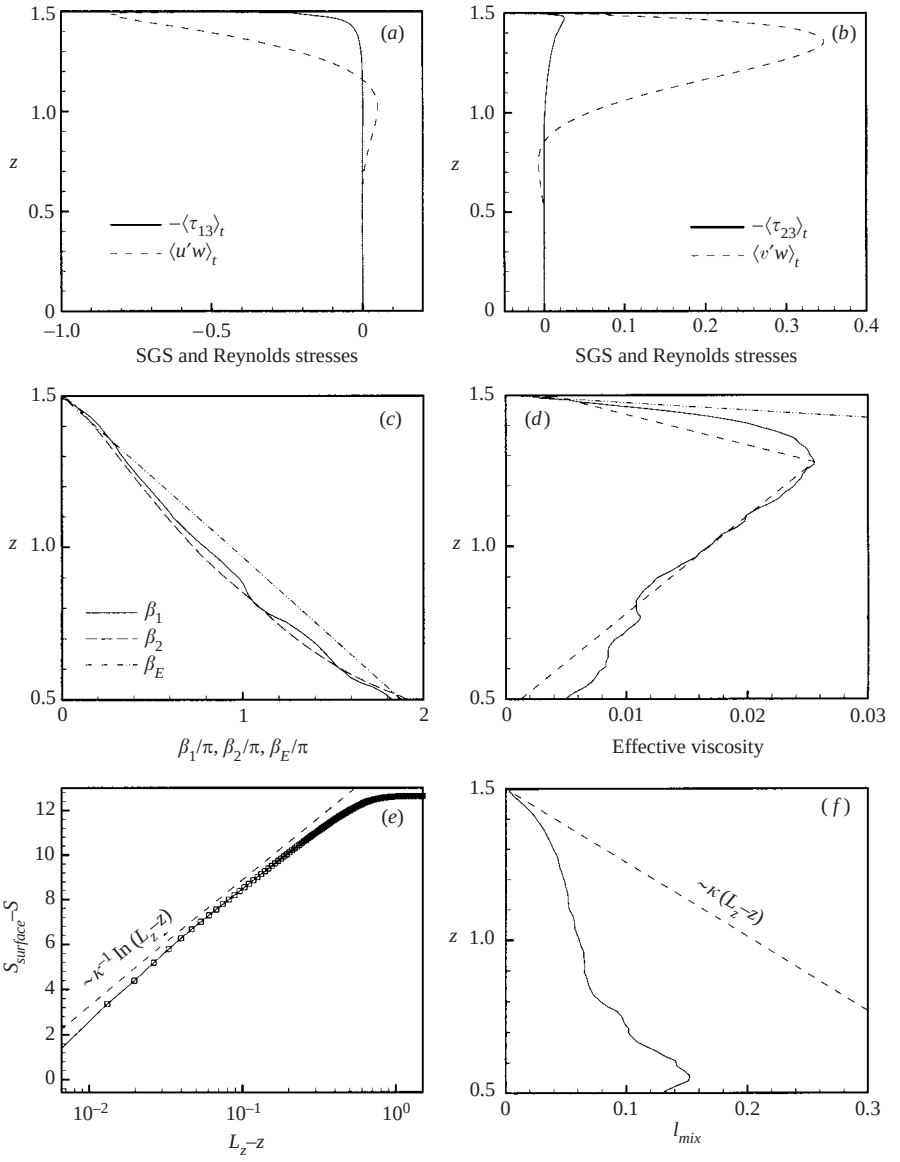

FIGURE 5. Horizontally and time-averaged profiles calculated in the developed turbulent flow at 90°-latitude. (*a*) x, z components of subgrid-scale and Reynolds stresses. (*b*) y, z components of subgrid-scale and Reynolds stresses. (*c*) angles between the wind direction and, correspondingly, the direction of the total stress vector (β_1), mean shear vector (β_2), and the shear vector in the Ekman solution (β_E). (*d*) ——, Effective viscosity coefficient (3.5) evaluated using the computed stress and shear profiles; – · · · – · · · –, linear dependence $A_z = \kappa(L_z - z)$ used by Madsen (1977); · · · · ·, constant-viscosity coefficient $A_{zE} = 0.0144$ of the Ekman model; – – –, piecewise-linear approximation of the viscosity profile used for an approximate solution (3.8). (*e*) Amplitude of the mean current vs. logarithm of depth. (*f*) Mixing length (3.6).

The result is shown in figure 5(*d*). The viscosity grows rapidly with depth and reaches its maximum at $z = L_z - 0.222$. Below this level, A_z decreases monotonically. No reliable evaluation could be performed below $z = 0.5$ because of the small amplitude of mean current and stress. For comparison, we plot the non-dimensional constant

effective viscosity $A_{zE} = 0.0144$ that has to be used in the Ekman model to achieve equal depth D for exponential decay of the speed of the current.

The effective viscosity profile in figure 5(d) is dissimilar to the depth-dependent distributions of A_z proposed earlier for the classical Ekman problem. For example, the entire profile cannot be approximated by a linear function (in our non-dimensional units) $A_z = \kappa(L_z - z)$, with von Kármán constant $\kappa = 0.41$ proposed by Madsen (1977). It is interesting to note, however, that in the thin subsurface layer the slope of calculated A_z is close to the von Kármán slope (see figure 5d). Madsen showed that an effective viscosity increasing with depth can produce a log-layer in the mean velocity profile. To verify this possibility we plot, in figure 5(e), the defect of the mean current amplitude as a function of $\ln(L_z - z)$. For comparison, a logarithmic line $\kappa^{-1}\ln(L_z - z)$ is shown. The log-layer behaviour is apparent in the subsurface region to the depth of, approximately, 0.2 of the turbulent length scale.

The closeness of the computed and logarithmic velocity profiles seems to indicate an agreement between our LES results and the classical similarity theory (e.g. Csanady 1967). We would like, however, to warn against drawing any far-reaching conclusions. The similarity theory is based on the existence of two independent length scales of the flow: the inner scale z_0, which can be the typical roughness of a rigid surface; or the viscous scale ν/u_*. The logarithmic profile is assumed in the region of overlap of inner (viscous) and outer layers. Our computations are performed in the limit of infinite Reynolds number, i.e. at $z_0 \to 0$. In this sense, we simulate only the 'outer layer' flow.

Csanady (1967) used the data of field measurements of the atmospheric Ekman layer in order to evaluate the theoretical constants. In particular, it was found that the shear angle α and the drag coefficient c_d are related as $\sin\alpha \approx 10.7(c_d)^{1/2}$. For our case, we take the angle between the surface current and shear stress $\alpha \approx 28.5^\circ$ and the drag coefficient $c_d \approx u_*^2/S_{surface}^2 \approx 0.00626$, which results in $\sin\alpha \approx 6.03(c_d)^{1/2}$. The agreement with Csanady's prediction is rather poor.

To compare our results with the model proposed by Rossby & Montgomery (1935) and other models based on the mixing-length assumption we evaluated the mixing length $l_{mix}(z)$ assuming that $A_z = l_{mix}^2[(\mathrm{d}\langle u\rangle_t/\mathrm{d}z)^2 + (\mathrm{d}\langle v\rangle_t/\mathrm{d}z)^2]^{1/2}$, which gives

$$l_{mix} = \frac{[(-\tau_{13} + \langle u'w\rangle_t)^2 + (-\tau_{23} + \langle v'w\rangle_t)^2]^{1/4}}{[(\mathrm{d}U/\mathrm{d}z)^2 + (\mathrm{d}V/\mathrm{d}z)^2]^{1/2}}. \tag{3.6}$$

The profile of l_{mix} is shown in figure 5(f). Here, the mixing length grows with depth but much slower than $\kappa(L_z - z)$ with $\kappa = 0.41$ predicted by Prandtl's theory. This result disagrees with the model of Rossby & Montgomery (1935) who assumed that the mixing length grows with depth in a thin boundary layer but monotonically decreases in the bulk flow.

3.3. *Solution for a piecewise-linear effective viscosity profile*

As we saw above, the mean horizontal current can be thought of as a solution of equations (2.12) for the averaged momentum with the depth-dependent effective viscosity $A_z(z)$ such as shown by the solid line in figure 5(d). One is tempted to try to find an analytical solution for $\langle u\rangle_t$, $\langle v\rangle_t$ using a plausible approximation of $A_z(z)$. A simple approximation is, of course, the piecewise-linear profile shown in figure 5(d). Three points of the $A_z(z)$ profile are used to plot the lines: the point next to the upper surface $z = L_z - 3.3\times10^{-3}$, where we took $A_z = 0.4\times10^{-3}$, point of the maximum $A_z = A_z^{max} = 0.256\times10^{-1}$ at $z = z_{max} = L_z - 0.222$, and the point at

$z = L_z - 0.492$, where we used $A_z = 0.17 \times 10^{-1}$. The approximation provides positive A_z to the depth of one turbulent length, i.e. at $z > L_z - 1$. Therefore, the solution below is valid in this area.

We introduce the complex velocity $W = \langle u \rangle_t + \mathrm{i}\langle v \rangle_t$ and the vertical coordinate z^* directed downward, and rewrite (2.12) as

$$\frac{\mathrm{d}}{\mathrm{d}z*}\left(A_z \frac{\mathrm{d}W}{\mathrm{d}z^*}\right) = \mathrm{i}W. \tag{3.7}$$

For A_z given by a linear function $az^* + b$, the general solution of (3.7) can be obtained in terms of Bessel functions

$$W = AJ_0(\chi) + BY_0(\chi), \tag{3.8}$$

where A and B are arbitrary complex constants and

$$\chi = (-1 + \mathrm{i})\zeta, \quad \zeta = \left(\frac{2z^*}{a} + \frac{2b}{a^2}\right)^{1/2}.$$

Alternatively, (3.8) can be expressed in terms of Kelvin's functions of real argument $\eta = 2^{1/2}\zeta$ as

$$W = C[\mathrm{ber}(\eta) + \mathrm{i}\,\mathrm{bei}(\eta)] + D[\mathrm{ker}(\eta) + \mathrm{i}\,\mathrm{kei}(\eta)]$$

with new arbitrary constants $C = A + \mathrm{i}B$ and $D = -2B/\pi$ (see Magnus, Oberhettinger & Soni 1966, p. 148).

To find A and B (or C and D) we apply the matching conditions at $z = z_{max}$, the boundary conditions

$$\frac{\mathrm{d}W}{\mathrm{d}z^*} = \frac{1}{A_z(0)} \quad \text{at} \quad z^* = 0$$

and $W = 0$ at some point deep in the column but still in the area where ζ is real.

We performed the procedure using the piecewise-linear viscosity profile described above and found the following approximate Bessel function solution for the Ekman layer on the f-plane:

$$W = (-28.0 + \mathrm{i}36.8)J_0(\chi_1) + (-36.7 - \mathrm{i}28.0)Y_0(\chi_1) \quad \text{if } z > L_z - 0.222, \tag{3.9}$$

$$W = (-0.047 - \mathrm{i}0.066)J_0(\chi_2) + (0.060 - \mathrm{i}0.036)Y_0(\chi_2) \quad \text{if } z < L_z - 0.222, \tag{3.10}$$

where

$$\chi_1 = (-1 - \mathrm{i})(20.3(L_z - z) + 7.6)^{1/2}, \quad \chi_2 = (-1 - \mathrm{i})(-63.9(L_z - z) + 66.3)^{1/2}.$$

To obtain a dimensional solution, the right-hand sides of (3.9) and (3.10) have to be multiplied by the velocity scale u_* and the coordinates χ_1 and χ_2 replaced by their dimensional counterparts

$$\chi_1^* = (-1 - \mathrm{i})(20.3z^*/L + 7.6)^{1/2}, \quad \chi_2 = (-1 - \mathrm{i})(-63.9z^*/L + 66.3)^{1/2}.$$

Here, z^* is the depth, the solution is defined at $Z^* < L$, with $L = u_*/f$ being the turbulent length scale.

The Bessel function solution (3.9) and (3.10) is illustrated in figures 1(b) and 6(a, b). The solution is considerably closer to the computed profile than the Ekman model solution. It is clear that one can achieve even better agreement by optimizing the coefficients a and b of the linear viscosity profiles.

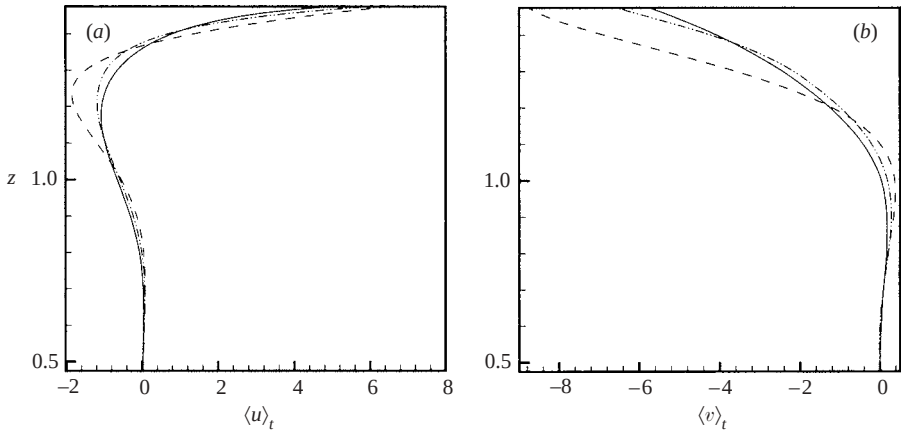

FIGURE 6. Comparison between the computed mean velocity profile (——), Ekman model (– · · – · · –), and the Bessel function solution (3.8) for the piecewise-linear effective viscosity (– – –). Horizontal components of the mean current are shown for the developed turbulent flow at 90°-latitude.

3.4. *Effects of latitude and wind direction*

In this section we deal with the possible effect of the tangential component $\boldsymbol{\Omega}_\tau$ of the Earth's rotation vector on the flow. Our discussion is based on a series of numerical experiments performed at different values of the latitude λ and the angle γ between the wind and the south–north direction (see figure 1*a*). In each experiment, we calculate the initial flow development for at least $2T_I$ and then collect the statistics for the time interval of $5T_I$.

The hodographs of mean currents obtained at $\lambda = 45°$, $\lambda = 15°$, and $\lambda = 90°$ are presented in figure 7(*a–c*). The shape of the current profile becomes increasingly dependent on the wind direction as the latitude decreases. In particular, the south-east (in the northern hemisphere) winds with $0 < \gamma < 90°$ correspond to the profiles with the velocity vectors turned more to the right in comparison with the f-plane case (larger angle between the wind direction and surface current), while the opposite winds with $180° < \gamma < 270°$ lead to the turn of the current more to the left. To quantify the transformation, figure 7(*d–f*) shows how the wind direction and latitude affect the angle $\alpha(L_z)$ between the surface current and the direction of the wind (figure 7*d*), the speed of the mean current at the surface $S(L_z)$ (figure 7*e*), and the depth of exponential decay of the current D, at which the speed is $S = S(L_z)\,\mathrm{e}^{-\pi}$ (figure 7*f*). It is interesting to see that the depth D differs significantly between the cases with south-east and north-west winds. The current amplitude decays much slower for $180° < \gamma < 270°$ than for the opposite wind directions. We will show below that this behaviour is caused by, respectively, increased or decreased vertical turbulent transfer of momentum.

At first glance, such a dramatic transformation of solutions with the latitude and wind angle is difficult to explain. Neither the equations (2.9) for the mean current nor the evolution equation for the turbulent kinetic energy contain any terms explicitly depending on λ or γ. The key idea that helps to understand the role of $\boldsymbol{\Omega}_\tau$ is recognition of the ability of the associated Coriolis force to affect the turbulent momentum transfer and to redistribute the turbulent kinetic energy between the velocity components. A general explanation of the underlying physical mechanism

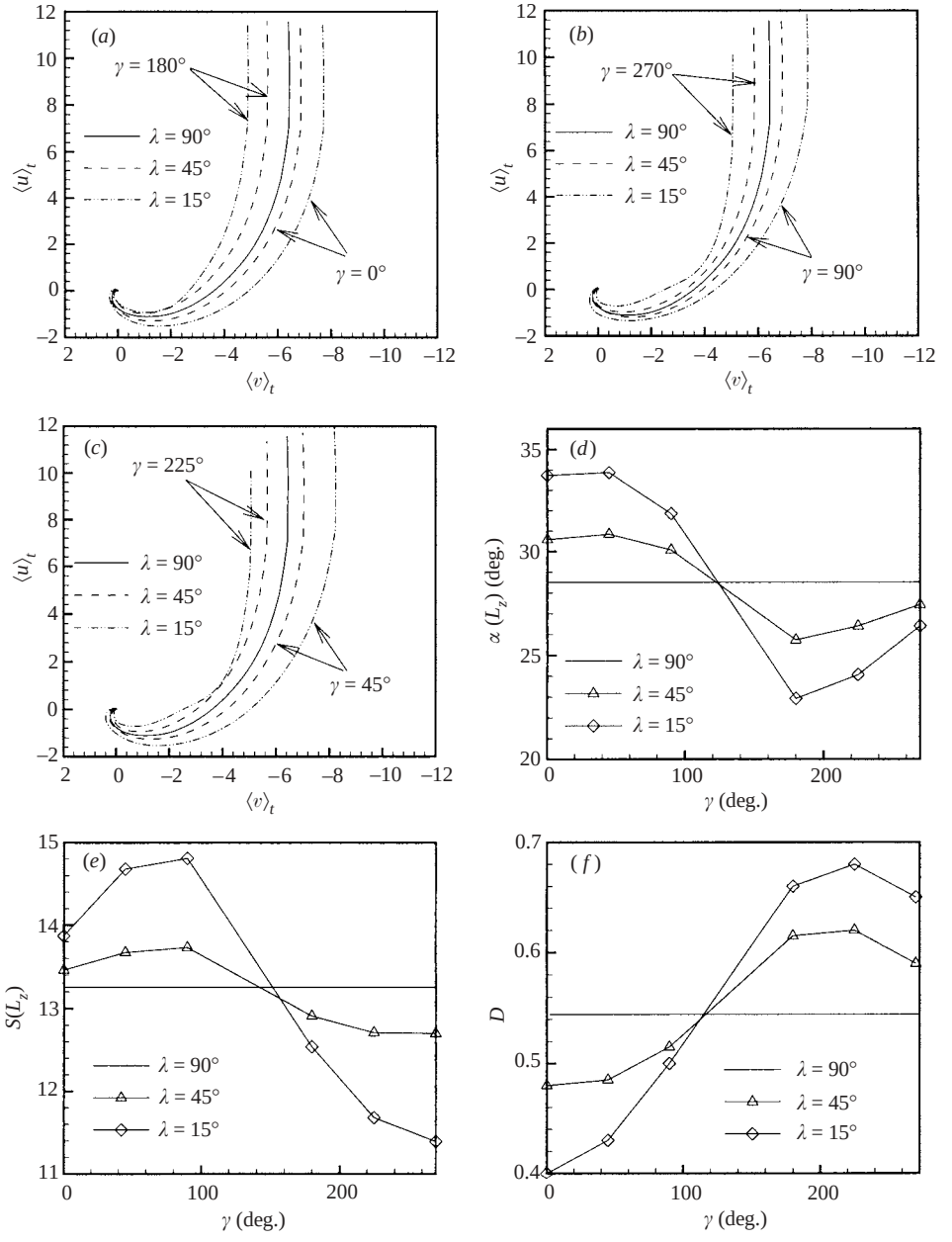

FIGURE 7. Impact of latitude λ and the wind angle γ on the mean velocity profile: (*a–c*) velocity hodographs; (*d*) surface angle $\alpha(L_z)$ between the current and the wind direction as a function of γ at different λ; (*e*) speed of the surface current $S(L_z)$; (*f*) depth of exponential decay of the current D.

can be found, for example, in Tritton (1978). It is based on the observation that the Coriolis force results in additional correlations between the vertical and horizontal turbulent velocity fluctuations.

To see the impact of tangential rotation we write the equations for the components of turbulent kinetic energy $\langle u'^2\rangle/2$, $\langle v'^2\rangle/2$, $\langle w^2\rangle/2$ and for the components $\langle u'w\rangle$,

$\langle v'w\rangle$ of vertical turbulent transport of the horizontal momentum:

$$\frac{1}{2}\frac{\partial}{\partial t}\langle u'^2\rangle = -\frac{\partial U}{\partial z}\langle u'w\rangle - 2\Omega_{\tau y}\langle u'w\rangle + \mathrm{OT}, \tag{3.11}$$

$$\frac{1}{2}\frac{\partial}{\partial t}\langle v'^2\rangle = -\frac{\partial V}{\partial z}\langle v'w\rangle + 2\Omega_{\tau x}\langle v'w\rangle + \mathrm{OT}, \tag{3.12}$$

$$\frac{1}{2}\frac{\partial}{\partial t}\langle w^2\rangle = 2\Omega_{\tau y}\langle u'w\rangle - 2\Omega_{\tau x}\langle v'w\rangle + \mathrm{OT}, \tag{3.13}$$

$$-\frac{\partial}{\partial t}\langle u'w\rangle = -2\Omega_{\tau y}[\langle u'^2\rangle - \langle w^2\rangle] + \mathrm{OT}, \tag{3.14}$$

$$\frac{\partial}{\partial t}\langle v'w\rangle = -2\Omega_{\tau x}[\langle v'^2\rangle - \langle w^2\rangle] + \mathrm{OT}. \tag{3.15}$$

Here we retained the non-negligible terms explicitly depending on $\Omega_{\tau x}$ and $\Omega_{\tau y}$ and the terms expressing the turbulence production by the mean shear. All the other terms, which are algebraically identical to the case with $\boldsymbol{\Omega_\tau} = 0$ are collected under the abbreviation OT (other terms). The $-$ and $+$ signs on the left-hand sides of (3.14) and (3.15) are chosen so that they correspond to time-derivatives of positive momentum transfer in the upper part of the flow domain.

Now we can see that the Coriolis force associated with the tangential rotation vector has a dual impact on the turbulent fluctuations. First, as seen in (3.14)–(3.15), it affects the vertical turbulent momentum transfers $\langle u'w\rangle$, $\langle v'w\rangle$ which, in turn, influence both the mean currents U, V (see (2.9)) and the turbulence production by the mean shear. Second, the Coriolis force redistributes the turbulent kinetic energy between the horizontal and vertical velocity components (see (3.11)–(3.13)).

The terms $-2\Omega_{\tau y}[\langle u'^2\rangle - \langle w^2\rangle]$ and $-2\Omega_{\tau x}[\langle v'^2\rangle - \langle w^2\rangle]$ in (3.14) and (3.15) can be considered as source/sink terms in the dynamic equations for the momentum transfers. All our computations confirmed that the horizontal velocity fluctuations are stronger than the vertical, i.e. $\langle u'^2\rangle > \langle w^2\rangle$ and $\langle v'^2\rangle > \langle w^2\rangle$ (see figure 4*d*). Thus, we have sources for both $-\langle u'w\rangle$ and $\langle v'w\rangle$ if $\Omega_{\tau x} < 0$ and $\Omega_{\tau y} < 0$, i.e. if $180^\circ < \gamma < 270^\circ$ and sinks if $\Omega_{\tau x} > 0$ and $\Omega_{\tau y} > 0$, i.e. $0^\circ < \gamma < 90^\circ$.

Our computations confirmed that, in agreement with the source/sink mechanism, the Coriolis force associated with $\boldsymbol{\Omega_\tau}$ significantly affects the vertical transfer of momentum. The transfer intensifies for $180^\circ < \gamma < 270^\circ$ and subsides for $0^\circ < \gamma < 90^\circ$, the effect increasing at lower latitude. An illustration is presented in figure 8(*a*, *b*).

The effect on the mean flow of increasing (decreasing) vertical momentum transfer can be expressed in terms of the increasing (decreasing) effective viscosity (3.5). We calculated $A_z(z)$ for each of the cases presented in figure 7 and found behaviour in agreement with this assumption. An example is in figure 8(*c*), which shows the $A_z(z)$-profiles for $\gamma = 45^\circ$ and $\gamma = 225^\circ$.

The redistribution of turbulent kinetic energy between the velocity components is another important aspect of the flow transformation caused by $\boldsymbol{\Omega_\tau}$. The energy is transferred from the horizontal to vertical velocity fluctuations if $\Omega_{\tau x}$ and $\Omega_{\tau y}$ are negative and in the opposite direction if they are positive. To illustrate this phenomenon figure 8(*d*) shows the ratio $2\langle w^2\rangle_v/\langle u'^2 + v'^2\rangle_v$ between the turbulent kinetic energy of vertical and horizontal velocity fluctuations as a function of γ at different λ.

The energy transfer from horizontal to vertical fluctuations at negative $\Omega_{\tau x}$ and $\Omega_{\tau y}$ does not mean that the energy of the horizontal fluctuations decreases. In fact, we

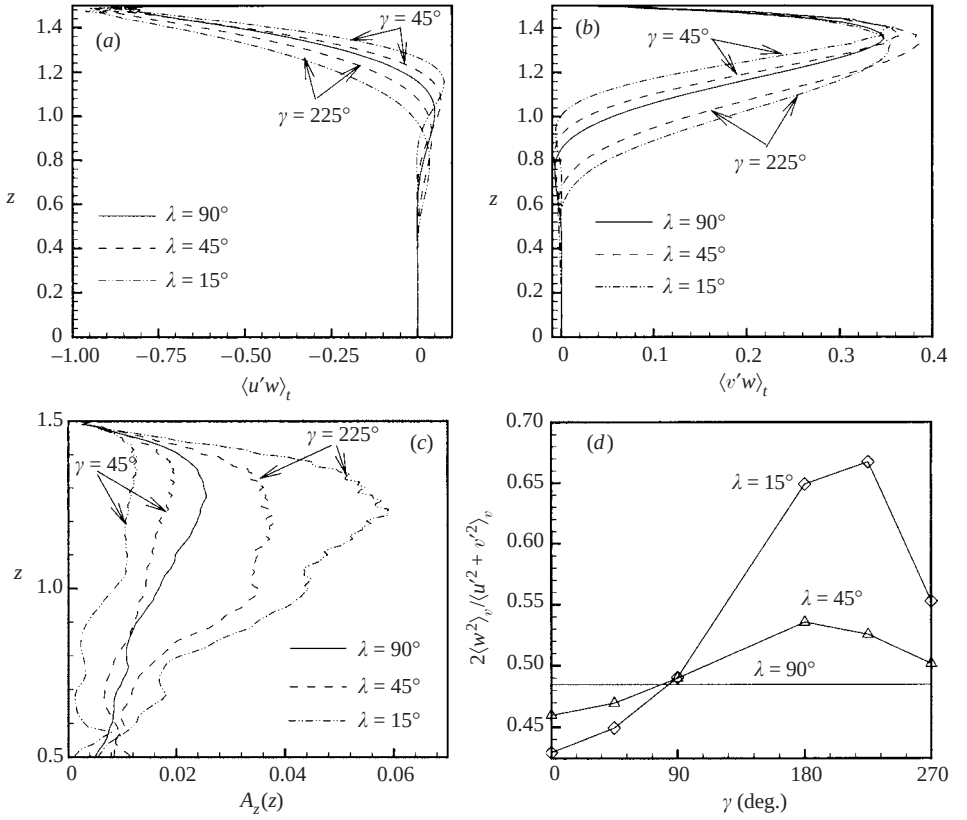

FIGURE 8. Effect of the latitude λ and wind angle γ on the properties of turbulent fluctuations. (*a*) x-component $\langle u'w\rangle$ of the turbulent momentum transfer; (*b*) y-component $\langle v'w\rangle$ of the turbulent momentum transfer; (*c*) effective viscosity $A_z(z)$; (*d*) ratio $2\langle w^2\rangle_v/\langle u'^2+v'^2\rangle_v$ between the volume- and time-averaged turbulent kinetic energy of vertical and horizontal velocity fluctuations.

found that it increases due to the growth of the turbulent momentum transfer $\langle u'w\rangle$, $\langle v'w\rangle$ that causes net growth of turbulence production by the mean shear. Also we found that the total non-dimensional turbulent kinetic energy $e=(\frac{1}{2})\langle u'^2+v'^2+w^2\rangle_v$ does not remain constant. One can see in figure 9(*a*) that it exceeds the f-plane level for $180^\circ<\gamma<270^\circ$ and drops below this level for $0<\gamma<90^\circ$.

Clearly, the increased (decreased) energy input into the turbulent fluctuations means corrections to the energy $E=(\frac{1}{2})\langle U^2+V^2\rangle_v$ of the mean flow. Figure 9(*b*) demonstrates that E increases with decreasing latitude if $0<\gamma<90^\circ$ and decreases if $180^\circ<\gamma<270^\circ$.

In order to finalize the discussion concerning the proposed mechanism through which $\boldsymbol{\Omega}_\tau$ influences the flow we will show that the modification of the turbulent momentum transfer can be responsible for the transformation of the shape of the mean current illustrated in figure 7. We will assume that the effect of enhanced (reduced) momentum transfer is expressed by increased (decreased) effective viscosity and use the Bessel function solution for a piecewise linear distribution of A_z.

An inspection of viscosity profiles in figure 8(*c*) reveals that the distinction potentially affecting the mean flow most is in the upper part of the profile where A_z increases with depth. The slope of $A_z(z)$ is defined by the value of the maximum

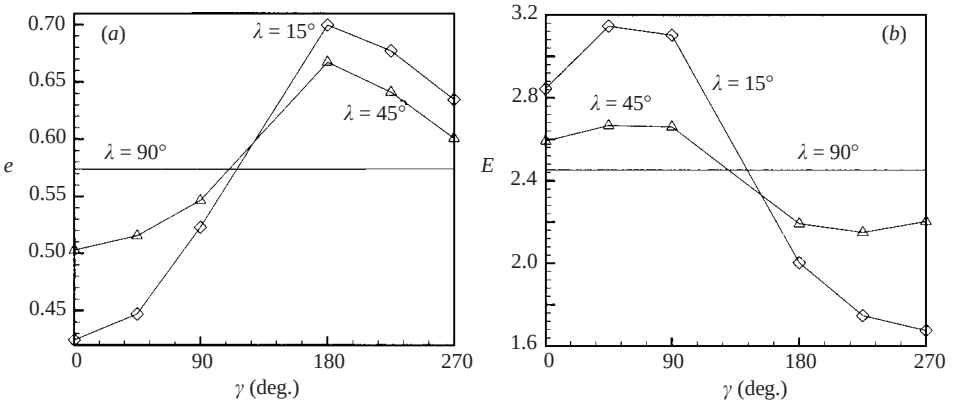

FIGURE 9. Effect of the latitude λ and wind angle γ on the flow energy: (a) energy of turbulent fluctuations $e=(\frac{1}{2})\langle u'^2+v'^2+w^2\rangle_v$; ($b$) energy of mean flow $E=(\frac{1}{2})\langle U^2+V^2\rangle_v$.

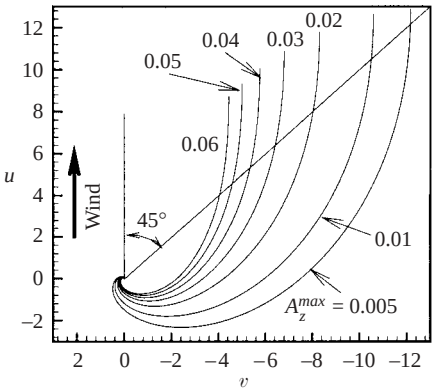

FIGURE 10. Velocity hodographs obtained as the Bessel function solutions (3.8) for $z_{max}=L_z-0.222$ and varying A_z^{max}.

effective viscosity A_z^{max} and the level z_{max} where this value is achieved. The lower part of the profile is believed to be less important since the mean flow and the fluctuations are much weaker in this area.

We calculated the Bessel function solutions for several piecewise-linear viscosity profiles. Each of them was defined using three points as follows. The upper point in all profiles was taken as in the f-plane case, i.e. $A_z=0.4\times10^{-3}$ at $z=L_z-3.3\times10^{-3}$. The difference between viscosity distributions was achieved through varying A_z^{max} (see the computed effective viscosity in figure 8c for comparison). The depth of maximum viscosity z_{max} was kept constant at $z_{max}=L_z-0.222$. To define the lower linear part of each profile we use the point $z=1$ and prescribed $A_z(1)=A_z^{max}-0.008$ for all cases except for the case with $A_z^{max}=0.005$ where we took $A_z(1)=0.001$.

The results presented in figure 10 clearly indicate validity of the proposed mechanism. Increasing A_z^{max} (i.e. enhancing effective viscosity) leads to the shift of the mean current to the left so that the angle between the current velocity and the wind becomes smaller at any depth. Another effect seen in figure 10 is the decrease of the current amplitude with increasing A_z^{max}. Both these effects are in agreement with the current modification observed in our experiments (see figures 7 and 9b).

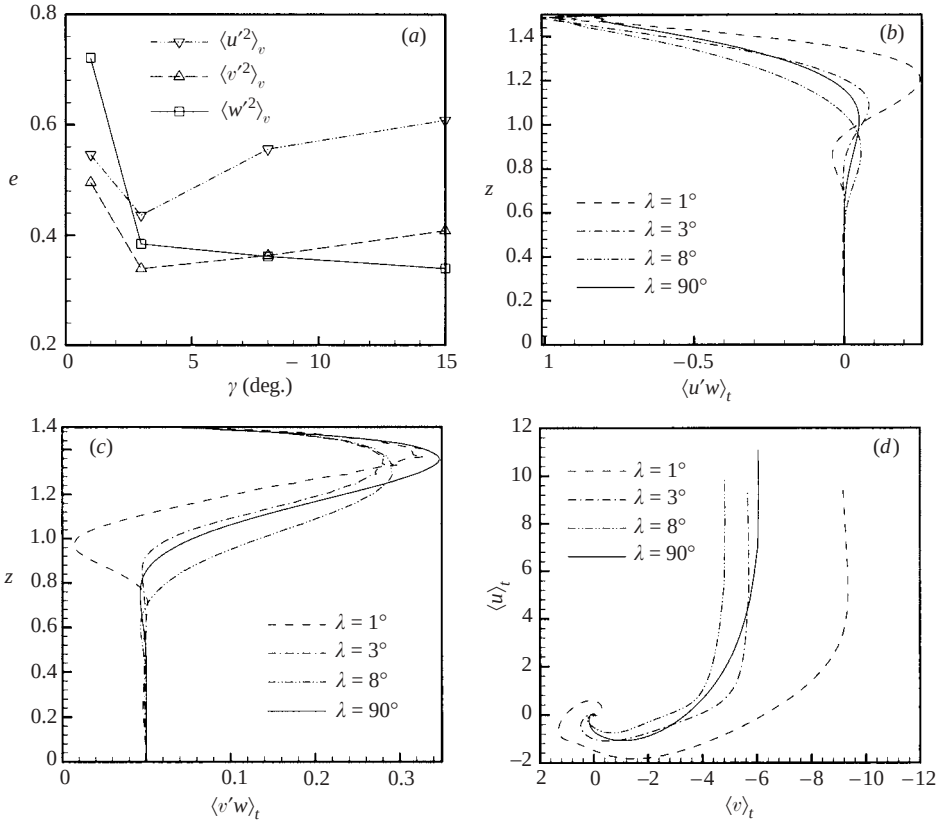

FIGURE 11. Effect of small latitude λ on the flow at the wind angle $\gamma = 225°$: (*a*) total energy of turbulent fluctuations $e = (\frac{1}{2})\langle u'^2 + v'^2 + w^2\rangle_v$; (*b*), *x*-component $\langle u'w\rangle$ of the turbulent momentum transfer; (*c*) *y*-component $\langle v'w\rangle$ of the turbulent momentum transfer; (*d*) velocity hodographs of the mean current.

3.5. *Flows near the equator*

Separate consideration should be given to flows in the equatorial zone, i.e. at $\lambda \to 0$. Some elementary consequences are the growth of the typical dimensional depth of the layer $L = u_*/f = 2u_*\Omega \sin\lambda$ and increase of the relative strength of the tangential rotation $\boldsymbol{\Omega_\tau}$. In addition to that, examination of equations (3.11)–(3.15) reveals modification of the mechanism by which the tangential rotation affects the flow. For the south–east winds with $0 < \gamma < 90°$, the effect of $\boldsymbol{\Omega_\tau}$ remains the same as at higher latitude. The associated Coriolis force suppresses the turbulent momentum transfer and redistributes the turbulent kinetic energy from vertical to horizontal fluctuations.

For north-west winds with $180° < \gamma < 270°$, however, the action of $\boldsymbol{\Omega_\tau}$ reverses as λ decreases below a certain level. At large negative $\Omega_{\tau x}$ and $\Omega_{\tau y}$, the energy transfer from horizontal to vertical fluctuations can lead to the situation where $\langle u'^2\rangle < \langle w^2\rangle$ and $\langle v'^2\rangle < \langle w^2\rangle$, thus converting the first terms on the right-hand side of (3.14) and (3.15) into sinks of the turbulent momentum transfer. One may expect that the Coriolis force associated with large negative $\Omega_{\tau x}$ and $\Omega_{\tau y}$ will suppress the turbulent flow.

To verify this hypothesis we performed simulations at $\gamma = 225°$ and $\lambda = 1°$, 3°, and 8°. The results presented in figure 11 support the scenario outlined above. At $\lambda = 8°$, the flow is qualitatively similar to the flow at $\gamma = 15°$. However, as the latitude decreases

further, the average turbulent kinetic energy of the vertical fluctuations becomes approximately equal to the energy of the x- and y-fluctuations (at $\lambda = 3°$) and exceeds them at smaller latitude (see figure 11a). This clearly causes the suppression of the turbulent momentum transfer (figure 11b, c) and the shift of the velocity hodograph to the right (figure 11d).

4. Conclusion

In this paper we have investigated the turbulent Ekman layer generated by a steady wind stress applied at the water surface. The traditional formulation of the problem that ignores the effects of stratification, surface convection, and gravity waves was considered. In an extensive series of LES numerical experiments, we showed that even in this case the classical Ekman model does not adequately describe the mean current. The main causes for this are the inadequacies of the assumptions in Ekman's model of a constant effective viscosity coefficient A_z and of a flow that is not affected by the tangential component of the Earth's rotation vector ('f-plane' approximation). Our simulations confirm that neither of these assumptions is justified.

We found that the effective viscosity concept by itself is relevant for the mean flow but the viscosity A_z varies strongly across the layer. It grows with depth in a subsurface layer of thickness about $1/4$ the turbulent length scale u_*/f, reaches the maximum value of about $0.025{u_*}^2/f$, and subsequently decreases with depth. The simulations revealed that the effective viscosity variability results in a mean flow profile that deviates significantly from the Ekman spiral. For example, on the f-plane, the angle between the surface current and the wind was found to be 28.5°, which is in clear disagreement with Ekman's 45° prediction. A particularly strong difference was detected in the rate of decay of the computed current amplitude in the subsurface region that was much higher than predicted by the Ekman model.

In an attempt to reconcile the model and simulations, we approximated the depth distribution of the effective viscosity by a piecewise-linear function. This led to a simple Bessel function solution that demonstrated better agreement with the numerical results than the original Ekman model.

Numerical experiments performed with different latitude λ and wind angle γ revealed that the flow is strongly affected by the Coriolis force associated with the tangential component of the Earth's rotation vector. Both the mean current and turbulent fluctuations were found to depend on λ and γ. Perhaps, the most interesting aspect for oceanographic applications is that, except for the latitude of 90°, the maximum (minimum) vertical turbulent momentum transfer occurs for north-west (south-east) winds.

Our analysis confirmed the validity of the underlying physical mechanism proposed earlier by other authors, in particular by Tritton (1978). The two main constituents of the mechanism are the redistribution of the turbulent kinetic energy between the vertical and horizontal velocity fluctuations and the modification of vertical turbulent momentum transfer.

This work was initiated with support by the Office of Naval Research (grant # N00014-00-1-0218).

Appendix. Accuracy of numerical presentation

In this section we present results of test computations performed to verify the accuracy of our numerical model. An indication that the model accuracy is sufficient

is the fact that the computed components of the Ekman transport

$$U_E = \int_0^{L_z} \langle u \rangle_t \, \mathrm{d}z \quad \text{and} \quad V_E = \int_0^{L_z} \langle v \rangle_t \, \mathrm{d}z$$

are within 4% of the theoretical values 0 and 1. Further, more detailed, discussion of the effects of the vertical and horizontal dimensions of the domain, numerical resolutions, and the length of the interval used for time-averaging is presented below. Of course, it must be recognized that even after minimizing the impact of all these factors, the accuracy of our simulations remains affected by the uncertainty introduced through the use of a subgrid-scale closure model.

In our simulation, as in any idealized simulation, where the computational domain presents only a part of the real flow domain, the right choice of the size of computational domain becomes important. The vertical and horizontal dimensions have to be taken large enough to minimize the impact of the artificial boundary conditions on the flow behaviour.

The effect of the periodic boundary conditions in the horizontal directions can be evaluated from the two-point velocity correlations coefficients presented in figure 3. The correlations across the distances of $L_x/2$ and $L_y/2$ consistently fall below the 0.05 value. This indicates that the periodic boundaries do not impose any significant limitations on the evolution of developed turbulent flow. Furthermore, we performed low-resolution computations with double L_x and L_y. No significant change in the flow behaviour was detected. It must be noted, however, that some effect of the periodic boundaries was observed at the stage of initial spin-up of the flow. The effect was associated with short-term excitation of primary instability modes that had a typical length scale comparable with L_x and L_y. This phenomenon was disregarded since the study of the initial spin-up was not the purpose of our investigation.

The validity of the free-slip bottom boundary condition (2.5) is based on the assumption that both the mean current and the turbulent fluctuations decay almost completely in the lower part of the computational domain so that the bottom boundary condition is of no importance. The profiles in figure 4 show that the assumption of flow decay is correct. For further verification we performed test simulations in domains of different depth. Turbulent statistics for a developed turbulent flow in the f-plane were analysed on the interval of $2T_I$. The horizontal domain dimensions and numerical resolutions were as in the main computations discussed above. In the vertical direction, we used $L_z = 1$, 1.5, and 2.0 with the resolution, respectively, $N_z = 100$, 120, and 135. The same grid stretching parameter $Z = 1$ was used in all three experiments. Typical results are presented in figure 12(a, b). One can see that $L_z = 1$ is insufficient, while the statistical moments for $L_z = 1.5$ are virtually indistinguishable from those for $L_z = 2$. We can conclude that the effect of the bottom boundary condition on our results obtained with $L_z = 1.5$ is negligible.

We would like to stress that the 'safe' limits on the domain size defined above are valid only in the particular case of classical Ekman flow considered in this paper. They should be reconsidered when other flow effects are taken into account. In particular, density stratification will, probably, require replacing the free-slip boundary condition by, for example, a Rayleigh damping sponge layer (Durran *et al.* 1993) to absorb the internal waves. This can lead to the necessity of increased L_z. If Langmuir turbulence or surface-cooling-driven convection are to be included, one would have to expect development of large-scale coherent structures in the flow and, thus, be ready also to increase the horizontal size of the domain.

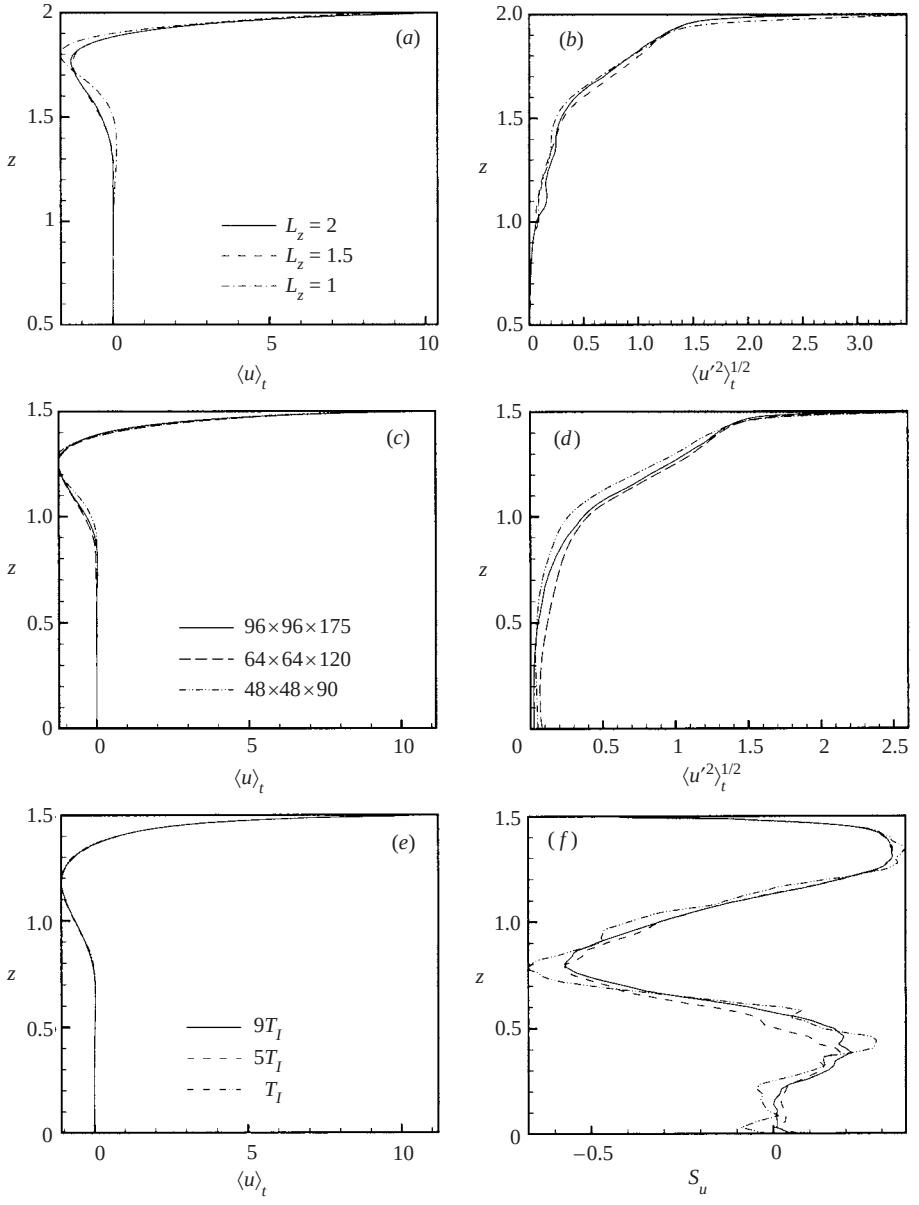

FIGURE 12. Verification of the accuracy of the numerical model. Horizontally and time-averaged profiles calculated in the developed turbulent flow at 90°-latitude: (a, b) mean velocity and r.m.s. perturbations calculated in the domains with different vertical size; (c, d) mean velocity and r.m.s. perturbations calculated with different numerical resolution; (e, f) profiles of mean velocity and skewness coefficient obtained by averaging over different time intervals.

For the LES model to be accurate in presenting the flow dynamics it should use a computational grid that is able to resolve the dominating turbulent vortical structures of the flow. In general, higher numerical resolution implies physically more relevant results even if the smallest scales of the flow are not resolved. To verify the sufficiency of our numerical resolution $N_x \times N_y \times N_z = 64 \times 64 \times 120$ we performed additional simulations with resolutions $48 \times 48 \times 90$ and $96 \times 96 \times 175$. The domain size was

$L_x \times L_y \times L_z = 1 \times 1 \times 1.5$. The flow on the f-plane was considered and the statistics were collected during $2T_I$ of the developed flow evolution. The results are illustrated in figure 12(c, d). Here, the first and second statistical moments are somewhat poorly represented in the simulation with the lowest resolution, while the difference between the profiles obtained with the two higher resolutions is small. A similar situation was observed for the third moments (not shown). We conclude that the accuracy of our $64 \times 64 \times 120$ simulations cannot be significantly improved by increasing the numerical resolution.

Finally, we discuss the effect of the time-averaging interval on the time- and horizontally averaged flow profiles. As discussed in § 3.2.1, the flow is subject to strong slow oscillations of a stochastic nature. The averaging interval should be taken large enough to minimize their effect on the collected statistics. We analysed this effect using the results of the f-plane numerical experiment described in § 3.2. The profiles of developed turbulent flow were obtained using different averaging intervals. The comparisons are illustrated in figure 12(e, f). The accuracy within 2% (in terms of relative error) in presenting the first and second statistical moments was achieved on averaging intervals as low as T_I or $2T_I$. For the skewness coefficients, longer averaging times were needed, especially to achieve convergence in the lower part of the domain. The period of $5T_I$ proved to be sufficient to provide a 2% level of accuracy at $1 < z < 1.5$ and 5% at $0.5 < z < 1$.

REFERENCES

Chereskin, T. K. & Roemmich, D. 1991 A comparison of measured and wind-derived Ekman transport at 11°N in the Atlantic ocean. *J. Phys. Oceanogr.* **21**, 869–878.

Coleman, G. N., Ferziger, J. H. & Spalart, P. R. 1990 A numerical study of the turbulent Ekman layer. *J. Fluid Mech.* **213**, 313–348.

Craik, A. D. D. & Leibovich, S. 1976 A rational model for Langmuir circulation *J. Fluid Mech.* **73**, 401–426.

Csanady, G. T. 1967 On the "resistance law" of a turbulent Ekman layer. *J. Atmos. Sci.* **24**, 467–471.

Ekman, V. W. 1905 On the influence of the earth's rotation on ocean currents. *Arch. Math. Astron. Phys.* **2**, 1–52.

Durran, D. R., Brown, R., Slinn, D. N. & Yang, M. J. 1993 Toward more accuarte wave-permeable boundary conditions *Mon. Weath. Rev.* **121**, 604–620.

Germano, M., Piomelli, U., Moin, P. & Cabot, W. H. 1991 A dynamic subgrid-scale eddy viscosity model. *Phys. Fluids* A **3**, 1760–1765.

Gnanadesikian, A. & Weller, R. A. 1995 Structure and instability of the Ekman spiral in the presence of surface gravity waves. *J. Phys. Oceanogr.* **25**, 3148–3171.

Langmuir, I. 1938 Surface motion of water induced by wind. *Science* **87**, 119–123.

Leibovich, S. & Lele, S. K. 1985 The influence of the horizontal component of Earth's angular velocity on the instability of the Ekman layer. *J. Fluid Mech.* **150**, 41–87.

Lilly, D. K. 1992 A proposed modification of the Germano subgrid scale closure method. *Phys. Fluids* A **4**, 633–635.

Madsen, O. S. 1977 A realistic model of the wind-induced Ekman boundary layer. *J. Phys. Oceanogr.* **7**, 248–255.

Magnus, W., Oberhettinger, F. & Soni, R. P. 1966 *Formulas and Theorems for the Special Functions of Mathematical Physics.* Springer.

McWilliams, J. C., Sullivan, P. P. & Moeng, C.-H. 1997 Langmuir turbulence in the ocean. *J. Fluid Mech.* **334**, 1–30.

Pond, S. & Pickard, G. L. 1993 *Introductory Dynamical Oceanography*, 2nd Edn. Bulterworth Heinemann.

Price, J. F. & Sundermeyer, M. A. 1999 Stratified Ekman layers. *J. Geophys. Res.* **140**, 20467–20494.

Price, J. F., Weller, R. A. & Pinkel, R. 1986 Diurnal cycling: Observations and models of the upper ocean response to heating, cooling, and wind mixing. *J. Geophys. Res.* **91**, 8411–8427.

Price, J. F., Weller, R. A. & Schudlich, R. R. 1987 Wind-driven ocean currents and Ekman transport. *Science* **238**, 1534–1538.

Rossby, C.-G. & Montgomery, R. B. 1935 The layer of frictional influence in wind and ocean currents. *Papers in Physical Oceanography and Meteorology* **III**, No 3. MIT and Woods Hole Ocean. Inst.

Schudlich, R. R. & Price, J. F. 1998 Observations of seasonal variation in the Ekman layer. *J. Phys. Oceanogr.* **28**, 1187–1204. *Pap. Meteorol. Oceanog.* **3**(3).

Scotti, A., Meneveau, C. & Fatica, M. 1997 Dynamic Smagorinsky model on anisotropic grid. *Phys. Fluids* **9**, 1856–1858.

Skyllingstad, E. D., Smith, W. D. & Crawford, G. B. 2000 Resonant wind-driven mixing in the Ocean boundary layer. *J. Phys. Oceanogr.* **30**, 1866–1890.

Slinn, D. N. & Riley, J. 1998 A model for the simulation of turbulent boundary layers in an incompressible stratified flow. *J. Comput. Phys.* **144**, 550–602.

Thorpe, S. 1984 The break-up of Langmuir circulation and the instability of an array of vortices. *J. Phys. Oceanogr.* **22**, 350–360.

Tritton, D. J. 1978 Turbulence in rotating fluids. In *Rotating Fluids in Geophysics* (ed. P. H. Roberts & A. M. Soward). Academic.

Walker, J. M. 1991 Farthest north, dead water and the Ekman spiral. Part II. *Weather* **46**(6), 158–164.

Weller, R. A. & Price, J. F. 1988 Langmuir circulation within the oceanic mixed layer. *Deep Sea Res.* A **35**, 711–747.

Zikanov, O., Slinn, D. N. & Dhanak, M. R. 2002 Turbulent convection driven by surface cooling in shallow water. *J. Fluid Mech.* **464**, 81–111.